Modelling of Air gap membrane distillation and its application in heavy metals removal

Hadi Attia [a], Muhammad S. Osman [b], Daniel J. Johnson [a], Chris Wright [a], Nidal Hilal [a*]

[a]Centre for Water Advanced Technologies and Environmental Research (CWATER), College of Engineering, Swansea University, Fabian Way, Swansea SA1 8EN, UK.

[b]Council for Scientific and Industrial Research (CSIR), Pretoria, South Africa.

*Corresponding author: n.hilal@swansea.ac.uk

Abstract:

In the present study, theoretical and experimental investigations were carried out to examine the effect of changing the operating parameters of an air gap membrane distillation (AGMD) system on the performance of electrospun and commercial membranes. These parameters include feed, cooling water temperature and feed flow rate. Analytical models were used, with the aid of MATLAB, to predict the permeate flux of AGMD based on heat and mass transfer. Heat transfer was used to predict the temperature on the membrane surface on the feed side and the thin film layer in the cooling plate on the air gap side, which was used later to calculate the vapour pressure and the permeate flux. The molecular diffusion model corresponded well with the experimental measurements in terms of predicting the permeate flux by varying the feed temperature, whilst it was poor in term of coolant temperature and feed flow rate. The results also illustrate that high rejection rates of around 99% of heavy metals can be achieved by using superhydrophobic electrospun membranes. The electrospun membrane flux increased with increasing feed tank temperature and flow rate while it was reduced with an increase of cooling line temperature.

Keywords:

Air gap membrane distillation, Experimental and theoretical studies, Superhydrophobic membrane, Heat and mass balance.

List of symbols

b	Air gap thickness	m
B_m	Thermally driven mass transfer coefficient	kg/m^2sPa
C_f	Feed concentration	mg/l
C_{mf}	Feed side membrane concentration	mg/l
de	Isopropanol density	g/m^3
dp	PVDF polymer density	g/m^3
D	Diffusion coefficient	ms^{-2}
h_f	Feed side heat transfer coefficient	$W\,m^{-2}K^{-1}$

h_m	Membrane heat transfer coefficient	$W\ m^{-1}K^{-1}$
h_p	Permeate heat transfer coefficient	$W\ m^{-2}K^{-1}$
H_v	Latent heat of vapourisation	$J\ kg^{-1}$
J	Water flux	$L\ m^{-2}h^{-1}$
k_{air}	Thermal conductivity of the air	$W\ m^{-1}K^{-1}$
k_f	Mass transfer coefficient	$m\ s^{-1}$
k_m	Thermal conductivity of the membrane	$W\ m^{-1}K^{-1}$
K_n	Knudsen number	-
M	Molecular weight	$g\ mol^{-1}$
p	Vapour pressure	Pa
p_{mf}	Vapour pressure at the feed membrane interface	Pa
P	Total pressure	Pa
P_a	Partial pressure of air in membrane pores	Pa
q_f	Feed flow rate	$ml\ min^{-1}$
q_p	Permeate flow rate	$ml\ min^{-1}$
Q	Heat flux	$W\ m^{-2}$
Q_f	Feed side convective heat flux	$W\ m^{-2}$
Q_m	Conductive heat flux through the membrane	$W\ m^{-2}$
Q_p	Permeate side convective heat flux	$W\ m^{-2}$
R	Universal gas constant	$J\ mol^{-1}K^{-1}$
T	Average temperature	K
T_f	Feed side inlet temperature	K
T_{mf}	Feed side membrane temperature	K
T_{mp}	Permeate side membrane temperature	K
T_{cd}	Thin film condensate temperature	K
T_{ca}	Cooling plate (permeate side) temperature	K
T_{cp}	Cooling plate (coolant side) temperature	K
T_p	Coolant water temperature	K
W_1	Saturated membrane with isopropanol weight	g
W_2	Dry membrane weight	g
τ	Membrane tortuosity	-
δ	Membrane thickness	m
ε	Membrane porosity	-
ρ	Density	$kg\ l^{-1}$

1. Introduction:

Membrane distillation (MD) is an emerging technology for water and wastewater treatment. It is based on phase change of the feed stream due to the application of thermal energy to the feed side and cooling to the product side of the membrane. This leads to a difference in the vapour pressure, which is the main driving force of the process. A hydrophobic membrane can be used to allow only the vapour to transfer, preventing passage of solutes. Air gap membrane distillation, which is one of four membrane distillation configurations (which also includes direct contact membrane distillation, vacuum membrane distillation, sweep gap membrane distillation), is based on using an air gap on the permeate side to reduce the heat lost by conduction and temperature polarization, increasing the effectiveness of the separation method [1].   In terms of AGMD, desalination is considered to be one of the major

applications for producing high quality water, particularly from sea water [2, 3]. However, AGMD can be used for other applications, such as treatment of oil-produced water [4], removal of dyes from textile wastewater [5] and other environmental waste water issues such as tackling of heavy metal contamination [6-8].

It is well documented in the literature that many parameters play a crucial role in hindering commercialization of membrane distillation, such as high energy consumption, shortage of high effectiveness membrane cells, low productivity and shortage of membranes with high hydrophobicity [9]. In terms of membrane hydrophobicity, many attempts have been made to overcome this problem, such as fluorosilanization of PVDF-SiO$_2$ blended membranes [10] and TiO$_2$ nanocomposite membranes[11], incorporation of carbon nanotubes (CNT) [12], use of PVDF-clay nanocomposites [13] and surface modification using a CF$_4$ plasma to increase membrane hydrophobicity[14]. However, the majority of these methods involve using silane and fluorinated groups which have potential environmental consequences [15]. Recently, a research group lead by Alexander [16] has suggested using alumina NP functionalized with environmentally friendly hydrocarbon branches instead of using silane and fluorinated groups to produce superhydrophobic surfaces. Based on this fact, Attia et al [8] reported fabrication of a superhydrophobic electrospun membrane using PVDF mixed with alumina NPs functionalized with isostearyl acids (hydrocarbon branch) with a WCA 150°.

Apart from membrane hydrophobicity, flux prediction in MD has gained great attention in recent years. In terms of AGMD modelling, the majority of work has been done by using one dimensional models to predict the permeate flux through hollow fibre or flat sheet membranes. The heat transfer model is similar for the two cases, but different models have been used to describe the mass balance. Ibarra-Bahena et al. [17] used the dusty-gas model (DGM) to calculate the mass transfer resistance for the membrane with a polytetrafluoroethylene (PTFE) flat sheet membrane with a pore size of 0.45 µm and air gap thickness of 3 mm. Alsaadi and colleagues [18] applied molecular diffusion and Knudsen diffusion in their model to calculate mass transfer resistance by using PTFE membrane. while Rochd et al [19] carried out a full simulation of AGMD by applying several mass resistance models (Knudsen, Molecular diffusion, Viscous diffusion, DGM, Schofield, KMPT, and KMT) to predict the pure water flux.

In this work, high lead concentrations were removed from feed water via AGMD by using a novel superhydrophobic electrospun membrane prepared from PVDF polymer and environmentally friendly superhydrophobic alumina. Furthermore, a modelling program was used to enhance membrane performance in terms of increasing the permeate flux. The model was used to predict membrane flux based on mass and heat transfer balance for AGMD and validated by experimental results. AGMD parameters, such as the effect of feed solution temperature, cooling water temperature and feed flow rate, were studied and applied to different models for father validation.

2. Model description and theory:

Modelling of the MD process has been accomplished most commonly for the DCMD configuration, which is considered the simplest and is the most often used. These models rely

on measuring the mass and heat resistance which simultaneously occur in the MD process. In the case of AGMD, the heat balance is used to predict the membrane surface temperature on the feed side as well as the temperature of the thin film of condensed water on the cooling plate in the air gap side.

In AGMD, mass transfer occurs by the movement of water molecules in the vapour phase through the membrane pores and this movement can be attributed to one of the following mass transfer mechanisms: Knudsen diffusion, Poiseuille flow (viscous flow), molecular diffusion, transition flow (which is a combined effect of Knudsen diffusion and molecular diffusion) and surface diffusion [20-22]. Knudsen flow dominates a MD system when there are frequent collisions between the water vapour molecules and the pore wall of the membrane [23, 24]. When the water vapour molecules collide with each other and, less frequently, with the membrane, Poisseuille flow occurs [23]. Whilst the collisions happen between water molecule and the pore wall, as well as collisions between water molecules and stagnant air molecules, molecular diffusion occurs [23, 25-27]. When modeling MD systems including AGMD systems, Poisseuille flow and surface diffusion are usually rendered insignificant [28, 29]. Figure 1 shows the temperature and vapour pressure profiles in AGMD.
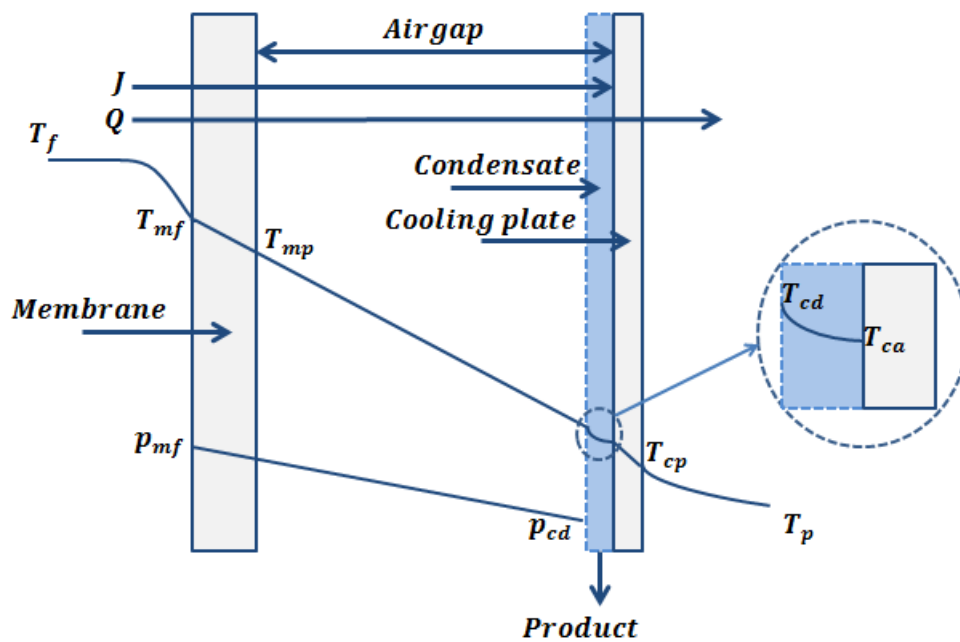

Figure 1: The temperature and vapour pressure profiles in AGMD.

In Figure 1, $T_f, T_{mf}, T_{mp}, T_{cd}, T_{ca}, T_{cp}$ and T_p are the feed side inlet temperature, the feed side membrane temperature, the air gap side membrane temperature, the thin film condensate temperature, the cooling plate (permeate side) temperature, the cooling plate (coolant side) temperature and the coolant temperature respectively. p_{mf} is the vapour pressure on the feed side of the membrane and p_{cd} is the vapour pressure on the condensate and can be calculated from the Antoine equation and from Raoult's law. J and Q are the water flux and the heat flux, respectively.

The water flux through the membrane and air gap, J, can be expressed as [30]:

$$J = B_m \Delta p = B_m(p_{mf} - p_{cd}) \qquad (1)$$

where B_m is the membrane coefficient and Δp is the vapour pressure difference across the membrane. The Knudsen number, K_n depicts the governing transport mechanism where upon, the membrane coefficient B_m is determined. K_n is defined as the ratio between the mean free path (S) of the water vapour molecules and the membrane pore diameter (r) and is shown mathematically in equation (2) [25]:

$$K_n = \frac{S}{2r} = \frac{k_B T}{2r \, \pi d_{vap}^2 P \sqrt{2}} \qquad (2)$$

where k_B is the Boltzmann constant, T and P are the temperature and total pressure, respectively and d_{vap} is the diameter of the vapour molecule. When $K_n > 1$, Knudsen diffusion dominates the migration of vapour molecules across the membrane and the water flux is calculated from equation (3) [27]:

$$J = \frac{2r\varepsilon\Delta p}{3(\tau\delta + b)}\left(\frac{8M}{\pi R T}\right)^{0.5} \qquad (3)$$

In equation (3) $\varepsilon, \delta, \tau, r$ and b are the membrane porosity, membrane tortuosity, membrane thickness, membrane pore radius and air gap thickness, respectively. M is the molecular mass of the water vapour; R and T are the universal gas constant and the average temperature between the feed side membrane temperature and thin film condensate layer respectively. When $K_n < 0.01$, molecular diffusion is the dominant mass transport mechanism [27]. Equation (4) is then used to calculate the water flux [31]:

$$J = \frac{\varepsilon PDM\Delta p}{(\tau\delta + b)RT(P_a)} \qquad (4)$$

P_a and D are the partial pressure of air in the membrane pores and the diffusion coefficient respectively. Transition flow occurs when $0.01 < K_n < 1$. Transition flow is the combination effect of both the Knudsen flow and molecular diffusion [25]. The water flux for transition flow can be calculated from equation (5) [25]:

$$J = \left(\frac{3(\tau\delta + b)}{2r\varepsilon}\left(\frac{\pi R T}{8M}\right)^{0.5} + \frac{(\tau\delta + b)RT(P_a)}{\varepsilon PDM}\right)^{-1}\Delta p \qquad (5)$$

Other models, such as the Dusty Gas Model (DGM), Knudsen-molecular diffusion-Poiseuille transition (KMPT) model and Knudsen flow Molecular Transition (KMT) model can be used for the MD application [19]. The DGM is one of the models frequently used to calculate MD fluxes [3]. It is considered to be a more complete model for all MD configurations as it combines all transport mechanisms through the membrane: Knudsen diffusion, molecular diffusion, surface diffusion and Poiseuille flow [32]. The DGM can be expressed as [19]:

$$J_{DGM} = \frac{(J_{MD} + J_K)J_P}{J_{MD} + J_K + J_P} \tag{6}$$

In equation (6), J_P is the Poiseuille flow water flux calculated from:

$$J_P = \left(\frac{0.125r^2 \varepsilon M(p_m)}{(\tau\delta + b)\mu RT} \right) \Delta p \tag{7}$$

where p_m is the partial pressure of air in the membrane pores [33]. Note that the Poiseuille flow may be negligible when the membrane pore size is small, i.e. less than 0.1µm [33]. Also of note is the Knudsen-molecular diffusion-Poiseuille transition model (KMPT), which takes into account the Poiseuille flow domination. The KMPT model is shown in equation (8)[19]:

$$J_{KMPT} = \frac{(J_{MD})J_K}{J_{MD} + J_K} + J_P \tag{8}$$

The exclusion of the Poiseuille flow reduces the KMPT model to the KMT model [4]:

$$J_{KMT} = \frac{(J_{MD})J_K}{J_{MD} + J_K} \tag{9}$$

Heat transfer during AGMD operation occurs as a result of the following phenomena: (i) convective heat transfer from the concentrated bulk feed to the membrane surface; (ii) water evaporation at the membrane surface; (iii) migration of water vapour molecules through the membrane and (iv) through the air gap; (v) water condensation on the condensing surface, where a cooling plate is typically used; (vi) heat convection through the condensate layer to the condensing surface; (vii) heat conduction through the condensing surface and lastly (viii) transfer of heat to the permeate/coolant.

Heat transfer from the concentrated feed to the membrane surface can be expressed as [2, 30]:

$$Q_f = h_f\left(T_f - T_{mf}\right) + J\,C_{pf}\left(T_f - T_{mf}\right) \tag{10}$$

where Q_f is the heat flux, h_f is the feed side heat transfer coefficient and C_{pf} is the specific heat capacity of the feed.

Heat transfer from the feed side membrane interface through the membrane pores and air gap to the condensate interface is given by equation (11) [30, 34]:

$$Q_m = \left(\frac{JC_{cd}}{1 - e^{-\frac{bJC_{cd}}{k_y}}} \right)\left(T_{mf} - T_{cd}\right) + JH_v \tag{11}$$

C_{cd}, H_v, b and k_y are the gas phase specific heat, latent heat of vapourisation, air gap thickness and gaseous thermal conductivity, respectively. Heat transfer through the condensate layer and cooling plate to the coolant liquid is given by [2, 30]:

$$Q_{cd} = h_{cd}(T_{cd} - T_{ca}) \tag{12}$$

$$Q_{cp} = \frac{k_{cp}}{l}(T_{ca} - T_{cp}) \tag{13}$$

$$Q_p = h_p(T_{cp} - T_p) \tag{14}$$

Equations (12-14) can be combined and expressed as[2, 30]:

$$Q_{cdp} = h_{cd}(T_{cd} - T_{ca}) = \frac{k_{cp}}{l}(T_{ca} - T_{cp}) = h_p(T_{cp} - T_p) = h_{cdp}(T_{cd} - T_p) \tag{15}$$

With
$$h_{cdp} = \left(\frac{1}{h_{cd}} + \frac{l}{k_{cp}} + \frac{1}{h_p}\right)^{-1}$$

h_{cdp} is the combined heat transfer coefficient, k_{cp} and l are the of the cooling plate thermal conductivity and thickness, respectively, while h_p is the permeate heat transfer coefficient and h_{cd} is the heat transfer coefficient of the condensate layer and can be calculated from [30]:

$$h_{cd} = \left(\frac{g\rho^2 H_v k_p^3}{L\mu_d(T_{cd} - T_{ca})}\right)^{0.25} \tag{16}$$

In equation (16) ρ is the condensate density and k_p is the condensate thermal conductivity. μ_d and L are the dynamic viscosity of the condensate and the cooling plate length respectively. At steady state:

$$Q_f = Q_m = Q_{cdp} \tag{17}$$

By combining equations (1), (10), (11), (15) and (17) and re-arranging, the following expressions for T_{mf} and T_{cd} can be obtained:

$$T_{mf} = T_f - \left(\frac{\left(\frac{1}{h_f} + \frac{1}{h} + \frac{1}{h_{cdp}}\right)^{-1}}{h_f}\right)\left((T_f - T_p) + \frac{JH_v}{h}\right) \tag{18}$$

$$T_{cd} = T_p + \left(\frac{\left(\frac{1}{h_f} + \frac{1}{h} + \frac{1}{h_{cdp}}\right)^{-1}}{h_{cdp}}\right)\left((T_f - T_p) + \frac{JH_v}{h}\right) \tag{19}$$

With
$$h = \frac{JC_{cd}}{1 - e^{-\frac{bJC_{cd}}{k_y}}}$$

These heat transfer coefficients (h_f) and (h_p) can be calculated from correlations available in the literature [35-37].

The feed concentration at the membrane surface is given by [38]

$$C_{mf} = C_f e^{\left(\frac{J}{\rho k_f}\right)} \tag{20}$$

where ρ is the feed density and k_f is the feed mass transfer coefficient.

Finally, a program was developed using MATLAB software (The MathWorks Inc, version R2016a, US) using the mass and heat balance equations mentioned above to predict the permeate flux. The model used a computational algorithm (Figure 2) which iteratively solves the equations using MATLAB. In addition, the development of the mathematical model was based on the following assumptions:

- The AGMD system is at steady state.
- Flow occurs in one dimension only.
- Only water vapour is transported through membrane pores.
- The air and water vapour in the pores are at equilibrium.
- There is no heat loss to the surroundings. Heat transfer occurs only in the AGMD system.
- A thin film layer of condensate forms of the cooling plate due to horizontal membrane cell configuration. Heat transfer through the film is by convection.
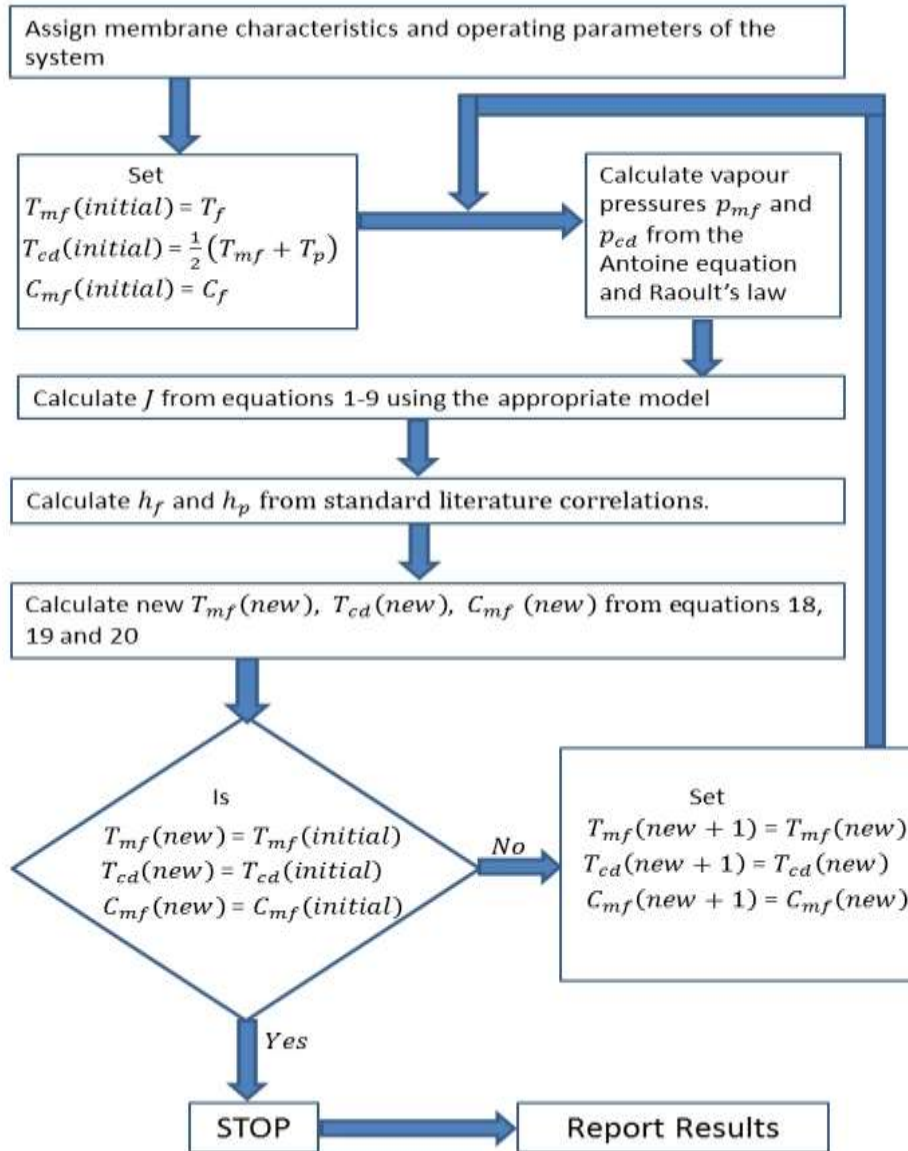- Pressure drop across the AGMD is negligible

Figure 2: Computational algorithm to numerically solve the mass and heat balance equations

3. Experimental study:
3.1. Fabrication of Electrospun membrane

Superhydrophobic electrospun membrane was made from polyvinylidene fluoride (PVDF) polymer with a molecular weight of 275,000 Da from Sigma Aldrich and superhydrophobic alumina. The membrane had a thickness around 100 μm and was fabricated using a homemade electrospinning machine as illustrated in Figure 3. The polymer solution was prepared by dissolving the polymer pellets in solvent mixture ratio 6:4 Dimethylformamide: Acetone, 0.05 wt%, cationic surfactant hexadecyl trimethyl ammonium bromide as well as 20 wt% of 13 nm alumina nanoparticles (Al_2O_3 NP) to polymer weight as previously reported by Attia et al [8] which were all purchased from Sigma Aldrich. Superhydrophobic Al_2O_3 NP was functionalized with isostearyl acids (Nissan Chemical Industries) according to the method reported by Shirin et al [16]. A heat-press with a temperature 160° C and pressure

6.27 kPa was applied to enhance membrane integrity by increasing the mechanical properties as well as to reduce membrane delamination.
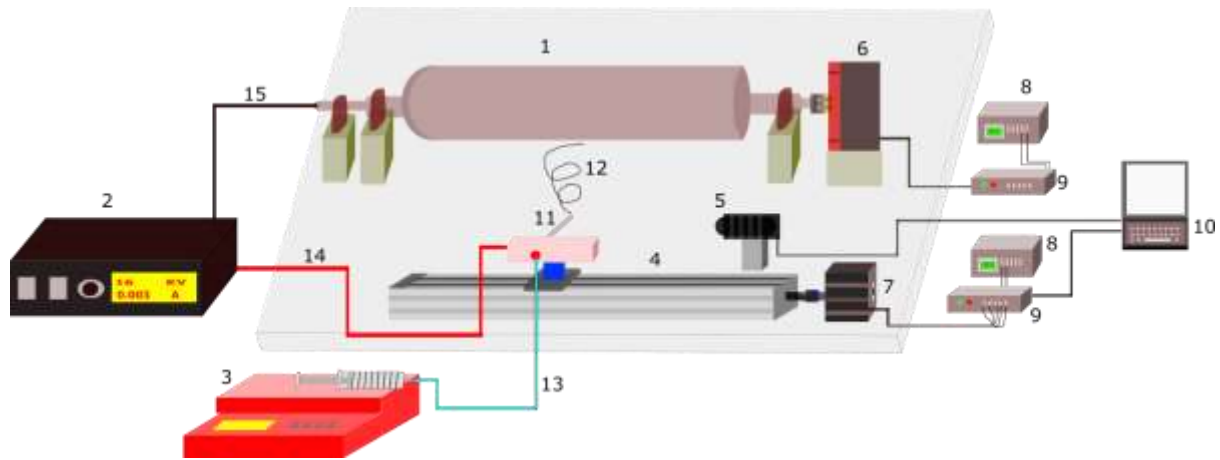

Figure 3: Schematic diagram of the drum Electrospinning device used in this study: (1) Aluminium drum, (2) HV power supply, (3) Syringe pump, (4) Actuator, (5) Camera, (6) Brushless motor, (7) Stepper motor, (8) Power supply, (9) Driver, (10) computer, (11) Needle, (12) electrospun fibre, (13) PTFE tube, (14) Positive HV wire, (15) Earth wire.

3.2. Membrane characterization

Non-woven electrospun membranes were characterized using different methods. Field emission scanning electron microscope (FE-SEM, S-7400, Hitachi, Japan) was utilized to scan the membrane surface. All membrane samples were sputter-coated with 5 nm of chromium (Quorum Q150TS, Quorum Technologies, UK). Image J program [39] was used to calculate the average fibre diameter from 100 distance measurements from SEM images.

Liquid entry pressure (LEP) was measured using a lab-made device, as shown in Figure 4a. An Amicon cell from Millipore with an effective surface area 13.4 cm^2 and capacity of 50 ml was used to accommodate the membrane. LEP was measured by placing a dry membrane in Amicon cell followed by increasing the pressure on the feed side of the membrane cell by 1 psi every 10 minutes, starting at 10 psi, using nitrogen gas. The value of the average of three pressure readings at which the first drop of DI water leaves the permeate side of the Amicon cell was recorded as LEP.

Membrane mean and maximum pore size were measured using the bubble-point method with a custom-made device (Figure 4b) which contained the same components as for the LEP test except using isopropanol solvent with surface tension of 21.4 dynes/cm to wet the ES membrane instead of DI water with a gas and bubble flowmeter to measure the gas flow rate on the permeate side.

Membrane porosity was evaluated by using a gravimetric method. The test was accomplished by weighing membrane samples (2 cm × 2 cm) before and after immersion into isopropanol solution for 10 minutes. Equation 21 was then employed to calculate the PVDF membrane porosity.

$$\varepsilon = \frac{(W_1 - W_2) \times \text{de}}{[(W_1 - W_2)/de] + \frac{W_2}{dp}} \qquad (21)$$

Where ϵ is the membrane porosity, W_1 is saturated membrane with isopropanol weight in gram, W_2 is the dry membrane weight in gram, de is the isopropanol density in (g/m^3) and dp is the PVDF polymer density in (g/m^3).

Membrane water contact angle (WCA) was measured using the sessile drop method. A Krüss model DSA25 device was used to measure the electrospun membrane WCA. Samples were immobilised onto a glass slide by a double sided adhesive tape. An average of five reading of the levelled dry membrane was taken.

Membrane thickness was measured using a digital micrometre with a precision of ±0.001 mm from Mitutoyo model 293 Series, IP65. An average reading of six measurements was used.
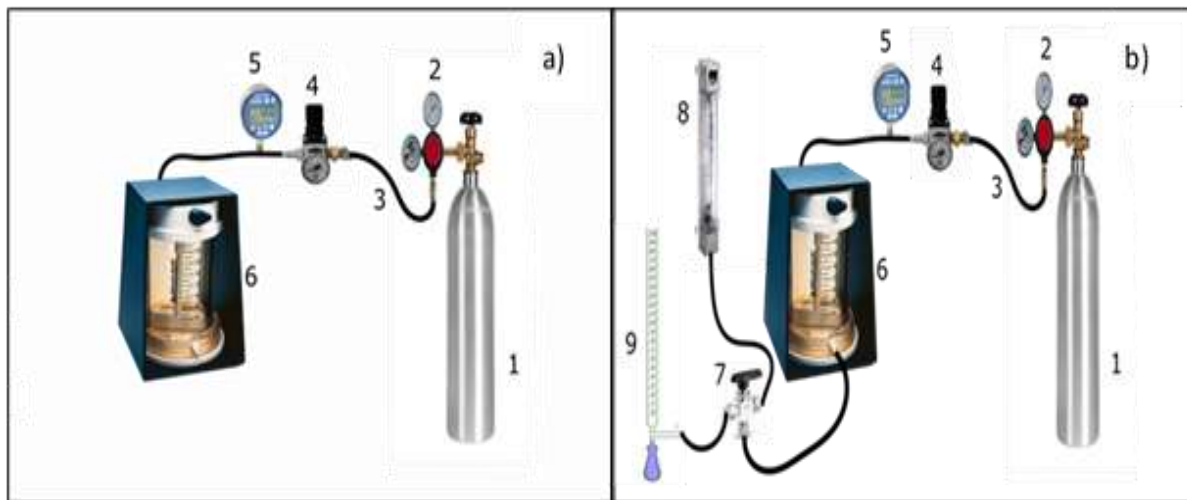

Figure 4 (a) lab-made LEP set-up apparatus, (b) Bubble point test set-up apparatus: (1) Nitrogen cylinder, (2) Regular valve, (3) hose, (4) needle valve, (5) Digital pressure gauge, (6) Amicon cell, (7) Two-way valve, (8) Gas flow meter, (9) Bubble flow meter.

3.3. AGMD set up

Commercial and electrospun membranes were tested by using a closed system custom-made AGMD unit. Figure 5 shows the AGMD unit which consists of four sections: feed tank, gear pump, stainless steel cell, thermocouples. The insulated feed tank has a capacity of 20 liter and is provided with a heater coil controlled by an Autotune temperature controller. Feed solution flow rate was controlled and pumped to the membrane cell through the glass flow meter from the feed tank by employing a gear pump (Tuthill Pump Co., UK). Stainless-steel tubing with outside diameter 6.35 mm used to circulate the feed and coolant liquid. Moreover, stainless steel membrane cell with a horizontal position was used. The membrane cell consisted of three parts: feed compartment; air gap compartment and cooling compartment. The outside dimension of the feed compartments is 145 × 95 × 55 mm (L × W × H), while the rectangular feed channel has a dimension of 520 × 4 × 3.2 mm (L × W × H)

which can accommodate a membrane with a surface area of 36.88 cm^2. A perforated aluminium plate with a dimension of 100×50 cm was used to support the membrane. The air gap width was 8.5 mm. The cooling compartment has the internal dimension $100 \times 50 \times 15$ mm (L $\times$W $\times$H), which was designed for providing pre-set cold water to the membrane cell with a flow rate of 8.5 l/min. Further, the feed and cooling water temperature was measured by using Four T- type thermocouples (TC Ltd). A TC-08 thermocouple data logger supplied by Pico technology was used to transfer the signals from thermocouple to the PC. Feed pressure was measured by using two analogue pressure gauges located around the membrane cell. An analytical balance (Precision Lab Balance) was connected to the PC and used to measure the weight of the permeate with time, allowing the permeate flux to be calculated. Microwave Plasma Atomic Emission Spectroscopy (MP-AES) model 4200 from Agilent technology was used to measure the lead concentration in the feed and permeate side and as a result calculate the rejection %. Feed solution was prepared by dissolving 1.614 g of Lead (II) nitrate from Fisher for each litre volume to obtain 1000 mg/l of lead solution for use in this experiment.
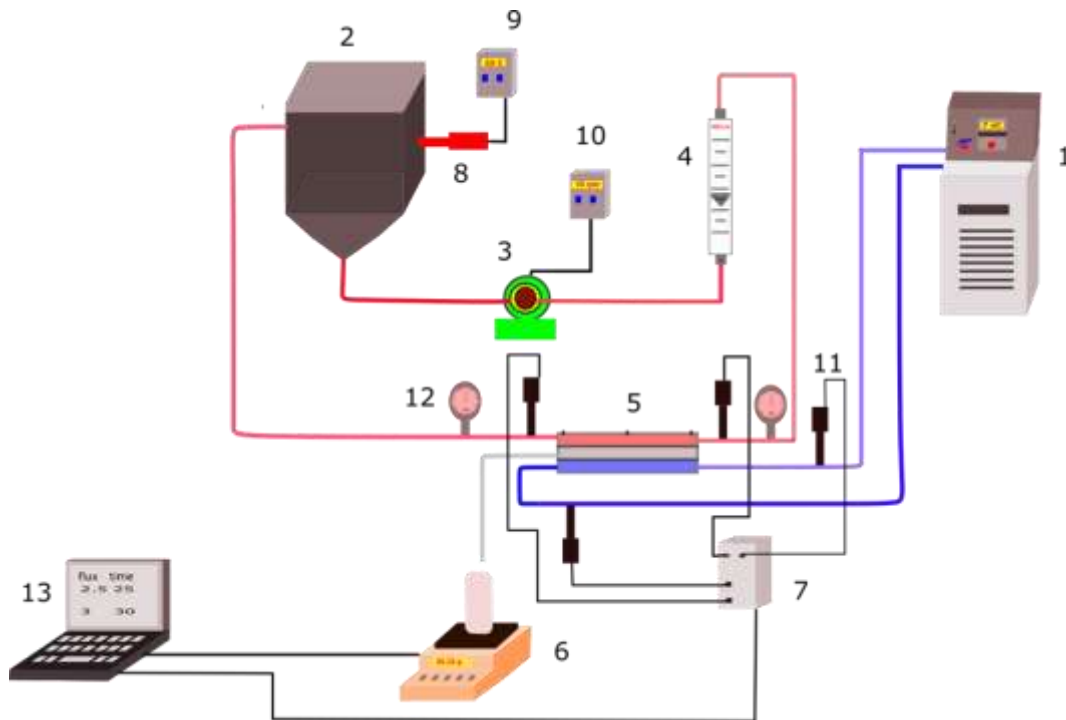

Figure 5: Schematic diagram of AGMD bench scale rig used in this study, (1) Chiller, (2) Feed tank, (3) Gear pump, (4) Flowmeter, (5) Membrane cell, (6) Electronic balance, (7) Thermocouple data logger, (8) Heater, (9) Heater controller, (10) Pump controller, (11) Thermocouple, (12) Pressure gauge, (13) Computer.

4. Result and discussion:

4.1. Membrane characteristics

Figure 6 shows an SEM picture of commercial and electrospun membranes which shows that the superhydrophobic alumina was attached to the external surfaces of the membrane fibres. The fibre distribution had a mean value of 105.6 nm (Figure. 6c). Figure 6d illustrates the surface topography of the commercial membrane examined. Additionally, Table 1 shows the characteristic of electrospun membrane, with a water contact angle of 150°, compared with 124° for commercial membrane, while the mean pore size is 0.37 µm for electrospun and 0.22µm for commercial membrane.
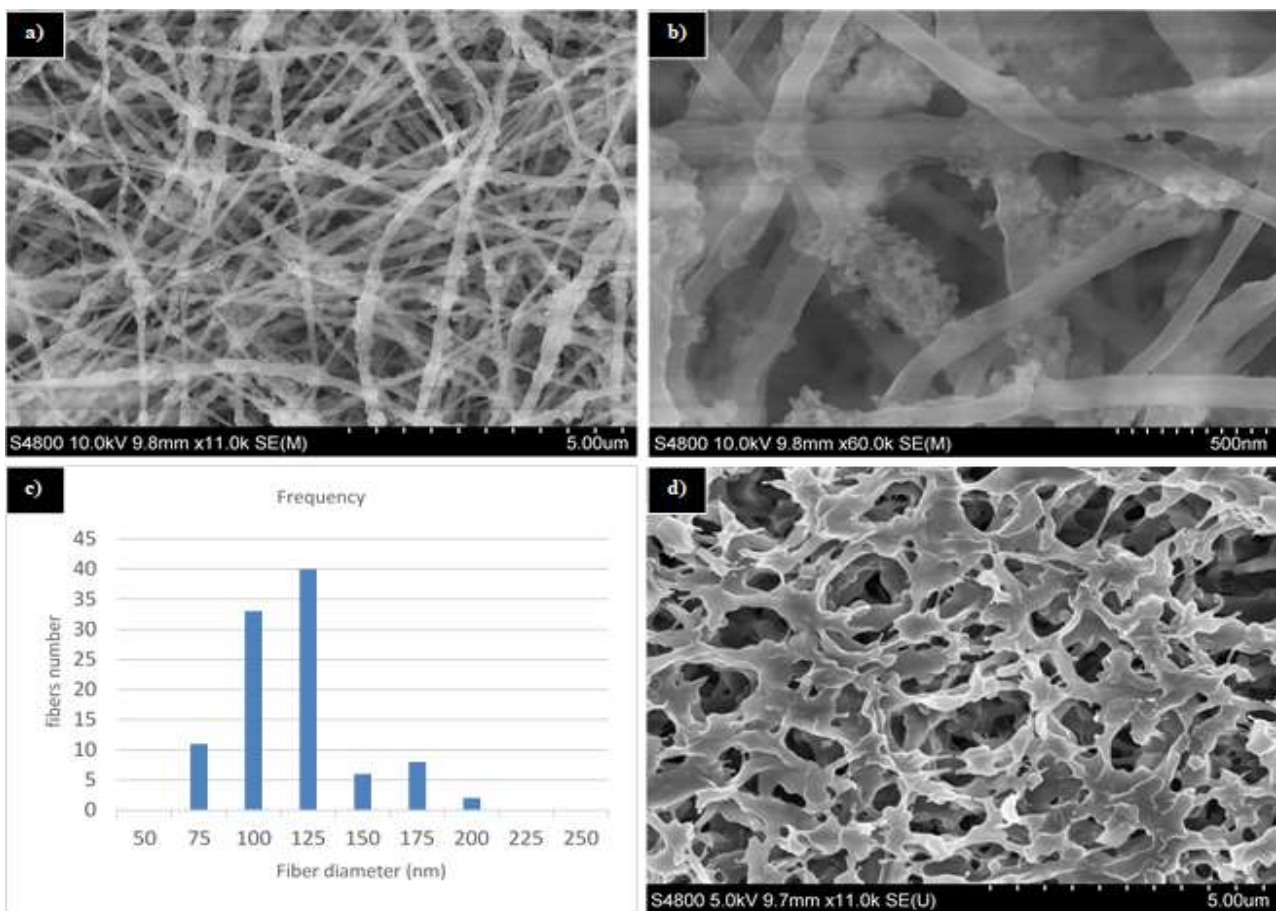

Figure 6: SEM pictures a) electrospun with 5 µm magnification; b) electrospun with 0.5 µm magnification; c) electrospun fibre histogram distribution; d) commercial membrane with 5 µm magnification.

Table 1: Characterization values of commercial and fabricated membranes.

Membrane code	Material	WCA, º	LEP, psi	Pore size, µm		Membrane thickness, µm	Porosity/ %	Mean fibre diameter, nm
				mean	max			
ES	11 wt% PVDF + 20 wt% Al$_2$O$_3$	150 ± 0.3	27	0.370	0.467	100 ± 3	0.912	**105.74**
GVHP	GVHP 29325	124 ± 0.2	30	0.220	-----	125 ± 2	0.75	-----

4.2. Effect of operation conditions on AGMD performance

4.2.1. Feed temperature

The impact of feed solution temperature on the AGMD flux for electrospun and commercial membrane using different theoretical models was examined. The experimental study was carried out by preserving other AGMD operating parameters at a constant value (coolant temperature 7°C and feed flow rate 1.5 L/min), while changing the feed temperature of the heavy metal solution from 30 to 70°C. Figure 7 shows the growth of the permeate flux in an exponential pattern when increasing the inlet feed temperature, which is due to the vapour pressure of the feed solution having an exponential relation with the feed temperature according to the Antoine equation. Moreover, Khalifa et al [30] pointed out that any slight change in feed temperature in the AGMD system leads to a direct effect on feed side vapour pressure which enhance the driving force across the membrane and corresponding increase the permeate flux. For example, increasing the feed temperature from 40 to 70° C enhances the permeate flux for electrospun membrane from 9.17 to 26.22 LMH respectively, which represented an increase of 185.93 % for electrospun membrane. For the commercial membrane, the increase was 290.27% by increasing the permeate flux from 5.86 to 22.87 LMH in the same feed temperature range. This result shows that the superhydrophobic membrane generate a higher flux: for instance, at 60°C the difference was 22% which might be due to slightly larger pore size, higher porosity and perfect wettability resistance. In terms of heavy metal removal all experiments showed rejection percentage of more than 99%.

The evolution of different models with the experimental result at different feed temperatures is shown in Figure 7 (a-d). It can be seen from Figure 7a and 7b that the experimental flux of the electrospun and commercial membranes fit firstly with the molecular diffusion and secondly with transition models. However, the Knudsen numbers fitted in the transition regime with values of 0.27 and 0.46 for electrospinning and commercial membrane, respectively. This might be attributed to limitation of these models in the present of the horizontal membrane cell due to not considering measurement of the condensate layer, which can affect both heat and mass transfer. Knudsen model predicted a high permeate flux, especially for electrospun membrane which might be due to higher porosity and pore size. In the case of the other models, Figure 7c, the experimental data fitted at lower temperature with DGM, while with the increase of feed temperature to more than 50°C it fitted between the

DGM and KMT model. While KMPT gave the highest permeate prediction compared with other models owing to this model being more affected by membrane characteristics, such as membrane pore diameter and thickness [40] [19]. Furthermore, in the case of commercial membrane the actual flux, as shown in Figure 7d, fit firstly with KMPT at feed temperatures less than 50°C which might be due to smaller pore diameter (0.22μm) compared with ES membrane (0.37 μm) and between KMPT and DGM with feed temperature above 50°C. To conclude, electrospinning and commercial membranes fit perfectly with the molecular diffusion and partial with DGM and KMPT models, respectively at temperature lower than 50°C.
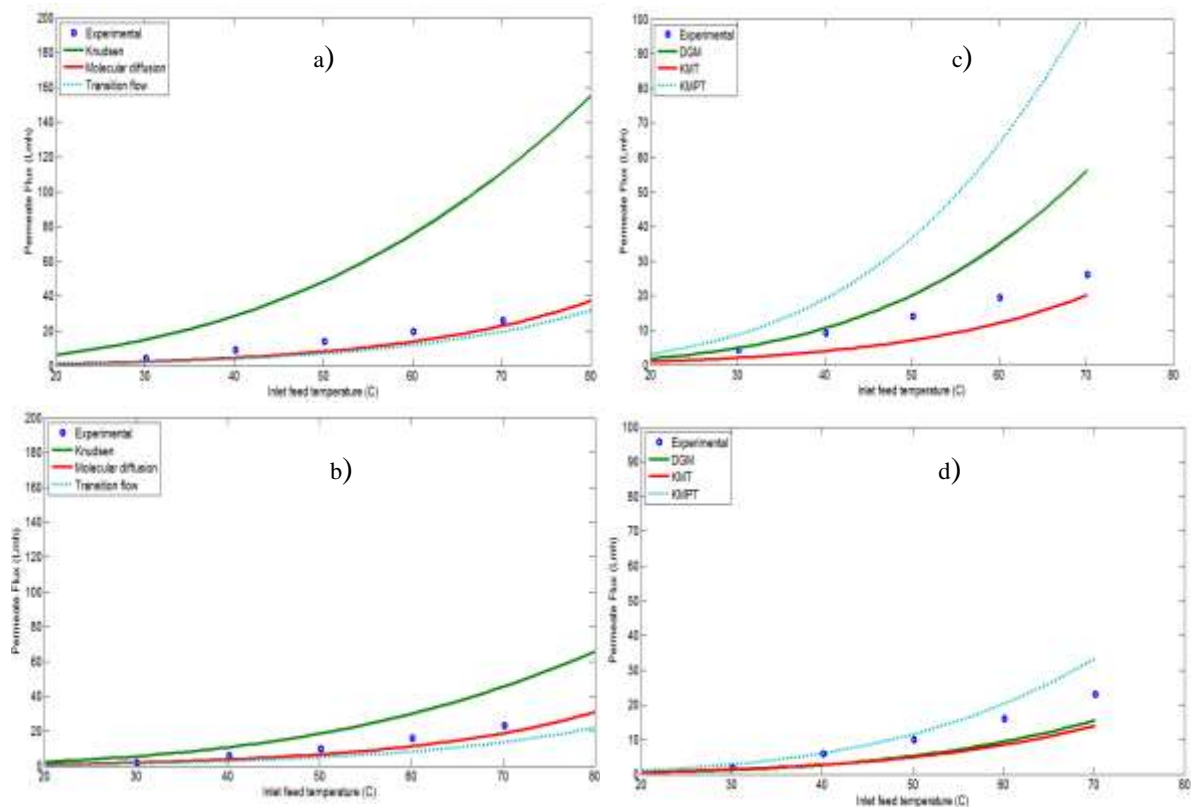

Figure 7: Permeate flux as a function of feed inlet temperature using (a-c) the electrospun membrane, (b-d) commercial membrane.

4.2.2. Cooling water temperature

Figure 8 illustrates the effect of varying the inlet temperature of coolant water on AGMD flux by using electrospun and commercial membrane. In this examination, the coolant line temperature was changed from 7 to 10°C then to 30°C by increasing in steps of 5°C. While keeping the other AGMD operation parameters constant (feed temperature at 60°C, feed flow rate 1.5L/min). In general, the permeate flux decreased slightly with the increase of coolant inlet temperature. For instance, the permeate flux decreased by 32.2% for electrospun membrane and 33.6 % for the commercial membrane when the inlet coolant line increased from 7 to 30°C. This can be attributed to a reduction of the driving force by the increasing vapour pressure on the permeate side. Furthermore, the increase of cooling plate temperature

might decrease the condensation rate of permeate vapour past the membrane. A similar result was gained by the Khalifa group [9] with an increase of 63% of flux measured when decreasing the coolant temperature from 25 to 10° C.

In terms of modelling, the results show stable theoretical permeate flux with varying of coolant temperature between 7 and 20° C. This can be explained by a negligible effect on driving force (pressure defence on both sides of the membrane) with a slight increase in vapour pressure on the permeate side with lower coolant temperature which is in agreement with the work of Banat et al [34]. Additionally, the underestimation of permeate flux for both models (molecular diffusion and transition models), especially when using electrospun membrane as shown in Figure 8a. For example, the predicted flux using the molecular diffusion model was lower by 30% to 7% when using a coolant temperature between 10 to 30° C. A similar disagreement between the experimental and theoretical flux prediction by varying the coolant temperature was obtained by Khalifa et al [31] and Banat et al [34]. Banat group explained that the disagreement between experimental and theoretical models at low coolant temperatures might be due to the increase of natural convection and sharp density gradients created by using a high temperature difference between feed and coolant side. Additionally, using a horizontal cell in this study might increase the disagreement between these models by increasing the natural conversion and density gradient due to the accumulation of condensate water on top of the horizontal cooling plate, before it discharges to the permeate, collector changing the air gap width (8.5mm). Beside electrospun membrane, the commercial membrane, Figure 8b, seems to have a better result in the range of coolant temperature between 25 and 30° C compared with the electrospun membrane, which might be due to the lower hydrophobicity of the commercial membrane.
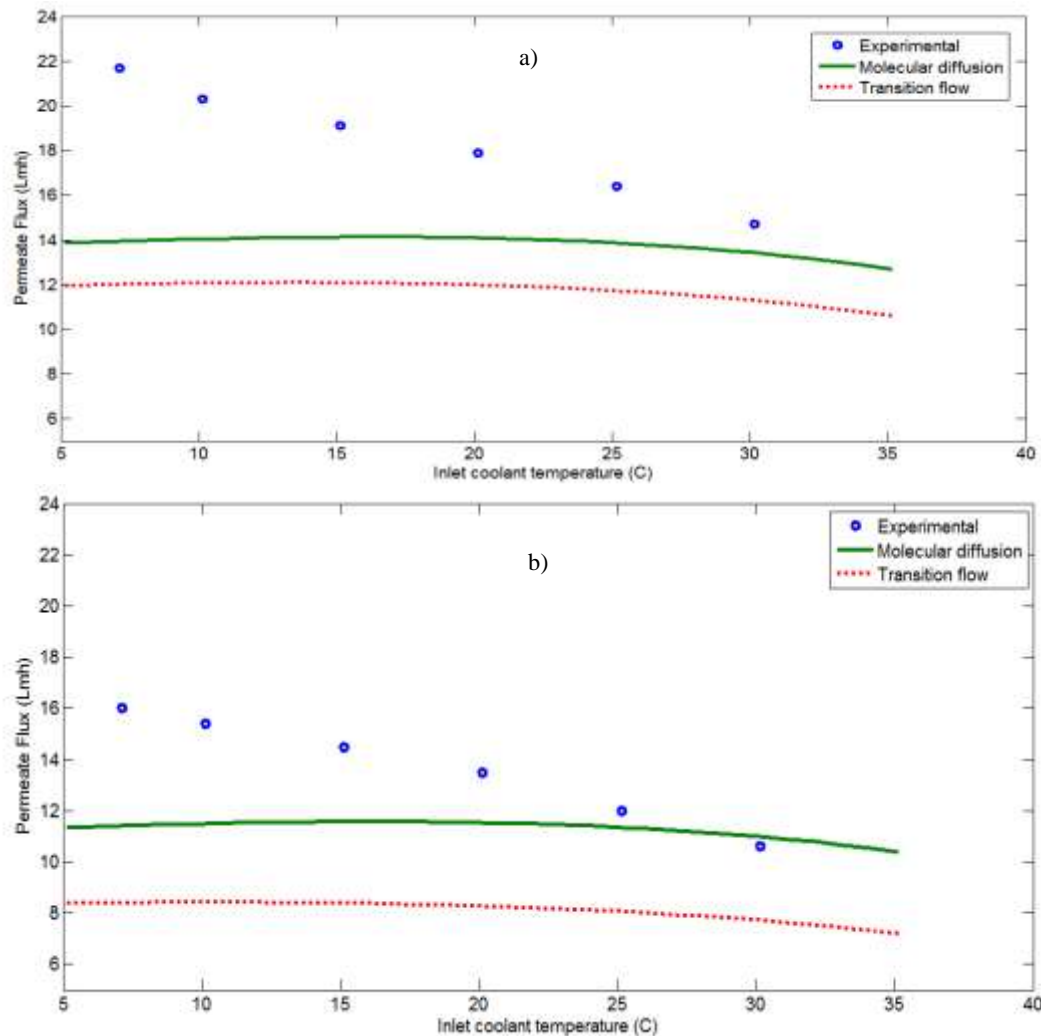
Figure 8: Permeate flux as a function of coolant inlet temperature using (a) the electrospun membrane, (b) commercial membrane

4.2.3. Feed flow rate

The effects of changing of feed flow rate on both the electrospun and commercial membranes are shown in Figure 9. The feed flow was changed from 0.5 to 1.5 L/min by 0.5 L/min increments, whilst keeping the other parameters constant, such as feed temperature (60°C) and coolant temperature (7°C). The results show that the flux increased by 14.18 % from 18.60 LMH for electrospun membrane and by 13.47% from 13.79 LMH for commercial membrane as the flow rate increased by 1 L/min from 0.5 L/min. This might be due to an increase of the heat transfer coefficient in the feed side from 70.6 to 723.4 W/m^2.K and diminution of the effect of heat and concentration polymerization in agreement with the work of Geng et al [41]. Furthermore, Banat group [34] showed that the membrane surface temperature could approach the feed bulk temperature by increasing the heat transfer coefficient. The theoretical predicted effect of an increase of feed flow rate on permeate flux by using molecular diffusion and the transition flow model, Figure 9, showed a small increase in the flux with inlet feed flow rate less than 15 l/h but reaches a plateau at high flow rates. According to both models, the flow pattern inside the feed channel was laminar with the

Reynolds number range from 62 to 1153, which led to an increase of the mass transfer coefficient of 11% for electrospun membrane and 8% for commercial membrane. However, the models underestimated permeate flux for both membranes, especially for the transition model. In term of membrane integrity and permeate quality, superhydrophobic electrospun membrane demonstrated acceptable mechanical properties by withstanding increased inlet pressure slightly due to increase of feed flow rate whilst preserving the rejection percentage (over 99%) without any evidence of wetting due to high LEP (~ 27 Psi) during five hour operating.
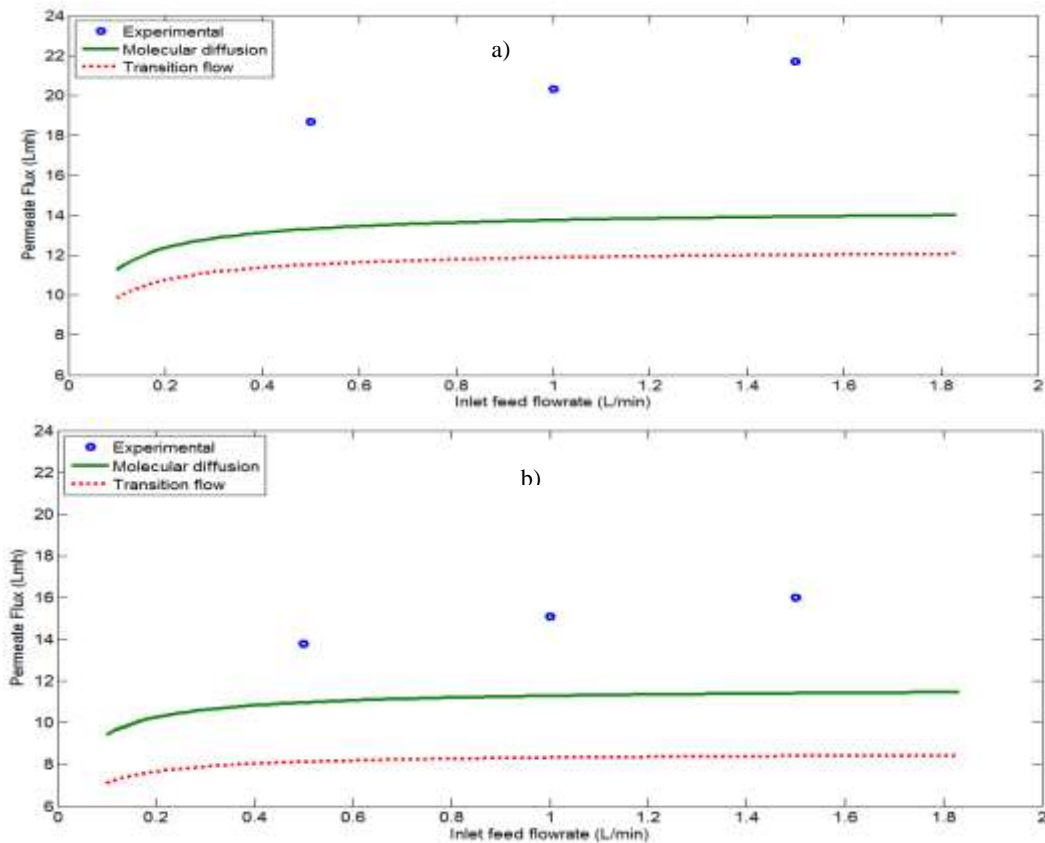

Figure 9: Permeate flux as a function of feed flow rate using (a) the electrospun membrane, (b) commercial membrane.

Conclusion:

An experimental and theoretical study was carried out on the AGMD configuration to improve the membrane performance in terms of flux and removal of heavy metal from artificial waste water. The research investigated the influence of different AGMD operation parameters on permeate flux, such as feed solution temperature, feed flow rate and coolant temperature. In addition, a comparison was made between commercial and a laboratory fabricated superhydrophobic membrane was investigated experimentally and theoretically. MATLAB program was used to assist in calculation of the membrane flux by using heat and mass balance models.

The experimental results showed that membrane flux increased exponentially with an increase of feed solution temperature and slightly with an increase of feed flow rate. However, the flux declined with an increase in coolant temperature and feed concentration. The rejection rate was above 99% for both commercial and electrospun membrane. The molecular diffusion model showed good agreement with both membranes in term of prediction of permeate flux with change of feed temperature compare with others models. However, an underestimation of flux was noticed by molecular diffusion with regard to the effect of coolant temperature and feed flow rate.

Acknowledgement

References

[1] M. Asghari, A. Harandizadeh, M. Dehghani, H.R. Harami, Persian Gulf desalination using air gap membrane distillation: Numerical simulation and theoretical study, Desalination, 374 (2015) 92-100.
[2] M.K. Souhaimi, T. Matsuura, Membrane distillation: principles and applications, Elsevier, 2011.
[3] M. El-Bourawi, Z. Ding, R. Ma, M. Khayet, A framework for better understanding membrane distillation separation process, Journal of Membrane Science, 285 (2006) 4-29.
[4] A. Alkhudhiri, N. Darwish, N. Hilal, Produced water treatment: Application of Air Gap Membrane Distillation, Desalination, 309 (2013) 46-51.
[5] G. Liu, C. Zhu, C. Cheung, C. Leung, Theoretical and experimental studies on air gap membrane distillation, Heat and mass transfer, 34 (1998) 329-335.
[6] A.M. Islam, Membrane distillation process for pure water and removal of arsenic, in, Chalmers University of Technology, Gothenburg, Sweden, 2004.
[7] P.P. Zolotarev, V.V. Ugrozov, I.B. Volkina, V.M. Nikulin, Treatment of waste water for removing heavy metals by membrane distillation, Journal of Hazardous Materials, 37 (1994) 77-82.
[8] H. Attia, S. Alexander, C.J. Wright, N. Hilal, Superhydrophobic electrospun membrane for heavy metals removal by air gap membrane distillation (AGMD), Desalination, 420 (2017) 318-329.
[9] A.E. Khalifa, S.M. Alawad, M.A. Antar, Parallel and series multistage air gap membrane distillation, Desalination, 417 (2017) 69-76.
[10] Z.-Q. Dong, X.-H. Ma, Z.-L. Xu, Z.-Y. Gu, Superhydrophobic modification of PVDF–SiO2electrospun nanofiber membranes for vacuum membrane distillation, RSC Adv., 5 (2015) 67962-67970.
[11] E.-J. Lee, A.K. An, T. He, Y.C. Woo, H.K. Shon, Electrospun nanofiber membranes incorporating fluorosilane-coated TiO 2 nanocomposite for direct contact membrane distillation, Journal of Membrane Science, 520 (2016) 145-154.
[12] M. Bhadra, S. Roy, S. Mitra, A Bilayered Structure Comprised of Functionalized Carbon Nanotubes for Desalination by Membrane Distillation, Acs Appl Mater Inter, 8 (2016) 19507-19513.
[13] J. Prince, G. Singh, D. Rana, T. Matsuura, V. Anbharasi, T. Shanmugasundaram, Preparation and characterization of highly hydrophobic poly (vinylidene fluoride)–Clay

nanocomposite nanofiber membranes (PVDF–clay NNMs) for desalination using direct contact membrane distillation, Journal of Membrane Science, 397 (2012) 80-86.

[14] C. Yang, X.-M. Li, J. Gilron, D.-f. Kong, Y. Yin, Y. Oren, C. Linder, T. He, CF 4 plasma-modified superhydrophobic PVDF membranes for direct contact membrane distillation, Journal of Membrane Science, 456 (2014) 155-161.

[15] M. Sagisaka, T. Narumi, M. Niwase, S. Narita, A. Ohata, C. James, A. Yoshizawa, E. Taffin de Givenchy, F. Guittard, S. Alexander, J. Eastoe, Hyperbranched hydrocarbon surfactants give fluorocarbon-like low surface energies, Langmuir, 30 (2014) 6057-6063.

[16] S. Alexander, J. Eastoe, A.M. Lord, F.d.r. Guittard, A.R. Barron, Branched hydrocarbon low surface energy materials for superhydrophobic nanoparticle derived surfaces, Acs Appl Mater Inter, 8 (2015) 660-666.

[17] J. Ibarra-Bahena, U. Dehesa-Carrasco, R. Romero, B. Rivas-Herrera, W. Rivera, Experimental assessment of a hydrophobic membrane-based desorber/condenser with H 2 O/LiBr mixture for absorption systems, Experimental Thermal and Fluid Science, (2017).

[18] A.S. Alsaadi, L. Francis, H. Maab, G.L. Amy, N. Ghaffour, Evaluation of air gap membrane distillation process running under sub-atmospheric conditions: Experimental and simulation studies, Journal of Membrane Science, 489 (2015) 73-80.

[19] Z.H. Rochd S, Mizani S, Dezairi A, Ouaskit S Modelisation of Membrane Distillation: Mass and Heat Transfer in Air Gap Membrane Distillation, J Membra Sci Technol 6(2016) 154.

[20] M. Tomaszewska, M. Gryta, A. Morawski, A study of separation by the direct-contact membrane distillation process, Separations Technology, 4 (1994) 244-248.

[21] M. Gryta, M. Tomaszewska, A. Morawski, Membrane distillation with laminar flow, Separation and Purification Technology, 11 (1997) 93-101.

[22] M. Tomaszewska, M. Gryta, A. Morawski, The influence of salt in solutions on hydrochloric acid recovery by membrane distillation, Separation and Purification Technology, 14 (1998) 183-188.

[23] Y. Mandiang, M. Sene, A. Thiam, D. Azilinon, Daily Estimate of Pure Water in a Desalination Unit by Solar Membrane Distillation, J Material Sci Eng, 4 (2015) 2169-0022.1000170.

[24] J. Mulder, Basic principles of membrane technology, Springer Science & Business Media, 2012.

[25] M. Qtaishat, T. Matsuura, B. Kruczek, M. Khayet, Heat and mass transfer analysis in direct contact membrane distillation, Desalination, 219 (2008) 272-292.

[26] S. Srisurichan, R. Jiraratananon, A. Fane, Mass transfer mechanisms and transport resistances in direct contact membrane distillation process, Journal of Membrane Science, 277 (2006) 186-194.

[27] A. Alkhudhiri, N. Darwish, N. Hilal, Membrane distillation: a comprehensive review, Desalination, 287 (2012) 2-18.

[28] T.Y. Cath, V.D. Adams, A.E. Childress, Experimental study of desalination using direct contact membrane distillation: a new approach to flux enhancement, Journal of Membrane Science, 228 (2004) 5-16.

[29] D. González, J. Amigo, F. Suárez, Membrane distillation: Perspectives for sustainable and improved desalination, Renewable and Sustainable Energy Reviews, 80 (2017) 238-259.

[30] A. Khalifa, D. Lawal, M. Antar, M. Khayet, Experimental and theoretical investigation on water desalination using air gap membrane distillation, Desalination, 376 (2015) 94-108.

[31] A.E. Khalifa, B.A. Imteyaz, D.U. Lawal, M.A. Abido, Heuristic Optimization Techniques for Air Gap Membrane Distillation System, Arabian Journal for Science and Engineering, 5 (2017) 1951-1965.

[32] N.N. Li, A.G. Fane, W.W. Ho, T. Matsuura, Advanced membrane technology and applications, John Wiley & Sons, 2008.

[33] Z. Ding, R. Ma, A. Fane, A new model for mass transfer in direct contact membrane distillation, Desalination, 151 (2002) 217-227.

[34] F.A. Banat, J. Simandl, Desalination by membrane distillation: a parametric study, (1998).

[35] L. Martínez-Díez, M.I. Vazquez-Gonzalez, Temperature and concentration polarization in membrane distillation of aqueous salt solutions, Journal of membrane science, 156 (1999) 265-273.

[36] M. Khayet, A. Velázquez, J.I. Mengual, Modelling mass transport through a porous partition: effect of pore size distribution, Journal of non-equilibrium thermodynamics, 29 (2004) 279-299.

[37] J. Phattaranawik, R. Jiraratananon, A. Fane, Effect of pore size distribution and air flux on mass transport in direct contact membrane distillation, Journal of Membrane Science, 215 (2003) 75-85.

[38] H. Kurokawa, O. Kuroda, S. Takahashi, K. Ebara, Vapor permeate characteristics of membrane distillation, Separation Science and Technology, 25 (1990) 1349-1359.

[39] C.A. Schneider, W.S. Rasband, K.W. Eliceiri, NIH Image to ImageJ: 25 years of image analysis, Nat Meth, 9 (2012) 671-675.

[40] Z. Ding, R. Ma, A. Fane, A new model for mass transfer in direct contact membrane distillation, Desalination, 151 (2003) 217-227.

[41] H. Geng, H. Wu, P. Li, Q. He, Study on a new air-gap membrane distillation module for desalination, Desalination, 334 (2014) 29-38.